Acta Cryst. (1996). B52, 414–422

A Synchrotron X-ray Study of the Electron Density in *C*-Type Rare Earth Oxides

E. N. MASLEN,[a] V. A. STRELTSOV[a]* AND N. ISHIZAWA[b]

[a]*Crystallography Centre, University of Western Australia, Nedlands 6907, Australia, and* [b]*Research Laboratory of Engineering Materials, Tokyo Institute of Technology, 4259 Nagatsuta, Midori-Ku, Yokohama 227, Japan. E-mail: strel@crystal.uwa.edu.au*

(*Received 2 June 1995; accepted 26 September 1995*)

Abstract

Structure factors for small synthetic crystals of the *C*-type rare earth (RE) sesquioxides Y_2O_3, Dy_2O_3 and Ho_2O_3 were measured with focused λ = 0.7000 (2) Å synchrotron X-radiation, and for Ho_2O_3 were re-measured with an Mo $K\alpha$ (λ = 0.71073 Å) source. Approximate symmetry in the deformation electron density ($\Delta\rho$) around a RE atom with pseudo-octahedral O coordination matches the cation geometry. Interactions between heavy metal atoms have a pronounced effect on the $\Delta\rho$ map. The electron-density symmetry around a second RE atom is also perturbed significantly by cation–anion interactions. The compounds' magnetic properties reflect this complexity. Space group $Ia\bar{3}$, cubic, Z = 16, T = 293 K: Y_2O_3, M_r = 225.82, a = 10.5981 (7) Å, V = 1190.4 (2) Å^3, D_x = 5.040 Mg m^{-3}, $\mu_{0.7}$ = 37.01 mm^{-1}, $F(000)$ = 1632, R = 0.067, wR = 0.067, S = 9.0 (2) for 1098 unique reflections; Dy_2O_3, M_r = 373.00, a = 10.6706 (7) Å, V = 1215.0 (2) Å^3, D_x = 8.156 Mg m^{-3}, $\mu_{0.7}$ = 44.84 mm^{-1}, $F(000)$ = 2496, R = 0.056, wR = 0.051, S = 7.5 (2) for 1113 unique reflections; Ho_2O_3, M_r = 377.86, a = 10.606 (2) Å, V = 1193.0 (7) Å^3, D_x = 8.415 Mg m^{-3}, $\mu_{0.7}$ = 48.51 mm^{-1}, $F(000)$ = 2528, R = 0.072, wR = 0.045, S = 9.2 (2) for 1098 unique reflections of the synchrotron data set.

1. Introduction

The physical properties of rare earth (RE) oxides are affected by the partial filling of their *f*-electron subshells. The *f* electrons are not involved strongly in chemical bonding and their effect on some physical properties is only of second order. Nevertheless, RE compounds have diverse magnetic properties, since on filling the RE atoms' *f* orbitals according to Hund's rules, the number of unpaired electron spins spans a wide range. Analysis of the influence of the crystal field and cation–cation interactions on RE oxide $\Delta\rho$ maps should assist our understanding of those magnetic interactions. Such studies require precise knowledge of RE oxides both with and without complicated magnetic interactions.

The RE sesquioxides can be hexagonal, monoclinic or cubic, denoted *A*-, *B*- and *C*-type, respectively, and follow the trend $A \rightarrow B \rightarrow C$ as the RE-atom radius decreases. The *C*-type sesquioxides have the mineral bixbyite (Mn_2O_3) structure, with two distinct cation sites that are attractive targets when assessing the effect of the crystal field on magnetic interactions.

The unique properties of mixed oxide garnets and perovskites containing RE atoms have been studied intensively. Coherent sequences of rare earth compounds are well suited to diffraction imaging with synchrotron radiation, which has evolved from a probe driven by scientific curiosity into a diagnostic tool for exploring crystal properties that were almost inaccessible previously. Synchrotron $\Delta\rho$ images for α-Al_2O_3 (Maslen, Streltsov, Streltsova, Ishizawa & Satow, 1993), α-Fe_2O_3 (Maslen, Streltsov, Streltsova & Ishizawa, 1994) and $YFeO_3$ (du Boulay, Maslen, Streltsov & Ishizawa, 1995) justify that confidence.

Metal–metal interactions beyond the range of normal chemical bonds influence crystal structure and electron densities strongly in RE compounds. Spin-dependent interactions play important roles in their magnetic ordering and structural transitions. Cation–cation effects are usually subordinate to the stronger cation–anion interactions with low RE-atom site symmetry. Local $\Delta\rho$ symmetry near the Y atom in $YFeO_3$ (du Boulay *et al.*, 1995) reflects the low-symmetry (C_s) crystal field due to neighbouring O atoms. Similar effects on $\Delta\rho$ images are expected around the RE2 cation sites with C_2 symmetry in the *C*-type RE sesquioxides. Crystal field and exchange interactions determine the magnetic moment and its anisotropy in those oxides. Consequently, Y_2O_3, Dy_2O_3 and Ho_2O_3 were studied here. At low temperatures Dy_2O_3 and Ho_2O_3 become antiferromagnetic, with complex spin ordering of uncertain origin. The Y^{3+} atom's closed-shell electron configuration is diamagnetic. The Dy^{3+} and Ho^{3+} atoms contain unpaired 4*f* electrons and impart paramagnetism to their oxides.

2. Experimental

Single crystals were prepared by flux-melting composites of RE_2O_3 + Al_2O_3 and PbO/PbF_2 in a platinum crucible with a tightly fitting lid, held at 1523 K for 1 h and then cooled at 5–7° h^{-1} to 1073 K, as described for rare earth oxyfluorides by Garton & Wanklyn (1968).

Aluminate crystals predominated after dissolving the flux in dilute HNO_3, but some garnets and oxides were also obtained. Crystal dimensions were measured and their faces indexed using optical and scanning electron Philips SEM505 microscopes. Colourless specimens with dimensions 51 × 20 × 30 (Y_2O_3), 23.1 × 30.6 × 22.9 (Dy_2O_3) and 18 × 31 × 32 μm (Ho_2O_3), measured from each crystal's centre, were bounded by two {100}, two {010} and two {001} faces. The Ho_2O_3 crystal has six truncated edges, each described by two {110}, $\{1\bar{1}0\}$, {101}, $\{10\bar{1}\}$, {011} and $\{0\bar{1}1\}$ faces, 32 × 32 × 31.5 × 31.5 × 41.5 × 41.5 μm, respectively, from the crystal centre. Transfer of lead from the flux into the crystals was assessed by electron-beam-induced X-ray microanalysis to be insignificant.

Diffraction intensities were measured with 0.7000 (2) Å synchrotron X-radiation using the BL14A four-circle diffractometer at the Tsukuba Photon Factory (Satow & Iitaka, 1989). The vertically polarized radiation was monochromated by twin Si (111) crystals and then focused using a curved mirror. The 0.95 polarization ratio is the fraction of the incident beam intensity with the electric vector vertical. A 0.4 mm diameter incident beam slit inserted before the monitor ion counter provided an adequately homogeneous intense beam. An ion chamber was used to monitor the incident beam flux variation due to the stored positron beam's decay. Positioning the specimen slightly off-focus minimized changes in the synchrotron radiation intensity due to particle beam instability. Alignment of the first monochromator crystal and the vertical translation of the mirror was optimized by automatic flux maximization every 20 min, stabilizing the incident beam intensity to within 1% over the 1 d data collection period.

Lattice constants were evaluated from six equivalent 20,0,0 reflections with 2θ values of 82.68 and 82.60° for Y_2O_3 and Ho_2O_3, respectively, and from six 10,0,0 and six equivalent 16,0,0 reflections at 2θ values of 38.31 and 63.31°, respectively, for Dy_2O_3.

Synchrotron reflection intensities for a reciprocal space sphere with $-23 \le h \le 23$, $-23 \le k \le 23$, $-23 \le l \le 23$ and $\sin(\theta/\lambda)_{max} = 1.0943$ Å^{-1} for Y_2O_3 and $\sin(\theta/\lambda)_{max} = 1.0929$ Å^{-1} for Dy_2O_3, and with $\sin(\theta/\lambda)_{max} = 1.0935$ Å^{-1}, $-23 \le h \le 23$, $-23 \le k \le 23$, $-23 \le l \le 16$ for Ho_2O_3 were measured systematically using $\omega/2\theta$ scans, with a 3 × 3 mm receiving slit in front of the NaI scintillation counter. The counter deadtime measured was 1.2 μs. Strong reflection intensities with count rates higher than 80 000 cps were reduced by Cu, Pt and Au foils with attenuation factors 17.99, 41.01 and 26.47 for Y_2O_3, Dy_2O_3 and Ho_2O_3, respectively. The diffraction intensities were corrected for deadtime counting losses using the Hester, Maslen, Spadaccini, Ishizawa & Satow (1993) polynomial expansion.

The lattice constant a = 10.605 (1) Å for Ho_2O_3 data set 2 was from 40 reflections with 13.34 < 2θ < 34.98°. All accessible Ho_2O_3 reflections were measured using Mo $K\alpha$ radiation (λ = 0.71073 Å) on a Syntex P3 four-circle diffractometer with an oriented graphite monochromator in the equatorial setting to $\sin(\theta/\lambda)_{max} = 1.0793$ Å^{-1}, $-22 \le h \le 15$, $-22 \le k \le 22$, $-22 \le l \le 22$. Six standard reflection intensities were remeasured every 100 reflections to monitor incident beam stability. Profile analysis (Streltsov & Zavodnik, 1989) allowed the weaker beams diffracted from the small crystal to be evaluated more accurately.

The measured intensities were modified and counting statistics variances adjusted for source instability as indicated by the standards (Rees, 1977). Variances consistent with Poisson statistics were retained. The other variances were increased according to the scatter of equivalents following a Fisher test. Further experimental details are set out in Table 1.

Lorentz and polarization were applied. The absorption corrections were analytical (Alcock, 1974), with μ coefficients evaluated from atomic values at 0.7 Å (Creagh, 1992) and for Mo $K\alpha$ (52.45 mm^{-1}) as listed in *International Tables for X-ray Crystallography* (1974, Vol. IV). The reference state for all structure-factor calculations was the independent atom model (IAM) using spherical atomic scattering factors from *International Tables for X-ray Crystallography* (1974, Vol. IV), with dispersion corrections $\Delta f'$ and $\Delta f''$ of –0.666 and 4.678 for Ho, 0.008 and 0.006 for O at Mo $K\alpha$, –2.338 and 3.478 for Y, –0.198 and 4.312 for Dy, –0.174 and 4.576 for Ho, and 0.011 and 0.006 for O at 0.7 Å, evaluated by Creagh (1992). All subsequent calculations utilized the *Xtal*3.2 system of crystallographic programs (Hall, Flack & Stewart, 1992) implemented on SUN SPARC and DEC 5000/120 workstations.

Before refining the structure, extinction corrections were evaluated from intensities for symmetry-related reflections with different path lengths (Maslen & Spadaccini, 1993). That unbiased algorithm provides a check on values that minimize differences between observed and calculated structure factors. However, non-physical corrections are sometimes obtained, because the mosaic distribution is non-uniform and beyond the scope of the simplest Maslen & Spadaccini algorithm. The extinction parameter determined for a sub-set of 783 strong reflections for the Ho_2O_3 SR data set included in Table 1 is significant, whereas the Y_2O_3 and the Ho_2O_3 tube data values were less than 1 e.s.d. The extinction parameter indicated for Dy_2O_3 was significantly negative.

More precise, although potentially biased, extinction corrections (Zachariasen, 1967) were evaluated by least-squares, optimizing the extinction corrections as part of the structure refinement using the formula of Larson (1970) (Refinement 1 in Table 1). The enormous extinction corrections determined contrast with the more reasonable estimates from symmetry-equivalent reflections. The large extinction parameter

Table 1. *Experimental and refinement data for Y_2O_3, Dy_2O_3 and Ho_2O_3*

	Y_2O_3	Dy_2O_3	Ho_2O_3	
Radiation	Synchrotron	Synchrotron	Synchrotron	Mo $K\alpha$
Diffractometer	PF†	PF	PF	Syntex $P3$
λ (Å)	0.7000 (2)	0.7000 (2)	0.7000 (2)	0.71073
Monochromator	Si(111)	Si(111)	Si(111)	Graphite
Scan speed (° min^{-1})	16	16	16	3.91
Peak scan width $[a + b\tan\theta]$ (°)	0.35; 0.0	0.20; 0.0	0.22; 0.0	1.75; 0.7
Maximum 2θ (°)	99.99	99.56	99.87	99.93
Maximum intensity variation of standards (*hkl*)	±(20,0,0), ±(0,20,0), ±(0,0,20)	±(18,0,0), ±(0,18,0), ±(0,0,18)	±(20,0,0), ±(0,20,0), ±(0,0,20)	±(222), ±(400), ±(044)
(%)	5.9	5.1	5.8	4.8
No of observed reflections	22 337	25 033	21 792	22 130
$[I > 3\sigma(I)]$	21 931	23 728	21 557	16 105
No. of independent reflections	1098	1113	1098	1042
Transmission range, min.; max.	0.117; 0.317	0.104; 0.255	0.098; 0.261	0.085; 0.238
Extinction‡, r^*	$\lvert - r^*\rvert < \sigma(r^*)$	$r^* < 0$	0.42 (9) × 10^4	$\lvert - r^*\rvert < \sigma(r^*)$
Min. extinction y§ (*hkl*)	–	–	0.58 ($\bar{2}22$)	–
R_{int} (F^2) (before,	0.144	0.155	0.121	0.148
after absorption)	0.059	0.066	0.050	0.098
Extinction applied	–	–	0.052	–
R	–	–	0.078	–
wR	–	–	0.041	–
S	–	–	8.3 (2)	–
$(\Delta/\sigma)_{max}$	–	–	0.6 × 10^{-4}	–
Refinement 1				
Extinction¶ refined, r^*	12.6 (2) × 10^4	4.2 (1) × 10^4	6.8 (1) × 10^4	7.2 (2) × 10^4
Min. extinction y§ (*hkl*)	0.21 (222)	0.36 (222)	0.31 (222)	0.31 (222)
R	0.022	0.016	0.016	0.027
wR	0.021	0.020	0.015	0.028
S	2.81 (6)	2.99 (6)	2.69 (6)	2.25 (5)
$(\Delta/\sigma)_{max}$	0.2 × 10^{-3}	0.4 × 10^{-1}	0.9 × 10^{-4}	0.4 × 10^{-4}
Refinement 2				
Extinction¶ refined, r^*	1.6 (3) × 10^4	0.39 (6) × 10^4	0.45 (9) × 10^4	0.43 (6) × 10^4
Min. extinction y§ (*hkl*)	0.58 (222)	0.62 (222)	0.59 (222)	0.60 (222)
R	0.067	0.056	0.072	0.083
wR	0.067	0.051	0.045	0.074
S	9.0 (2)	7.5 (2)	9.2 (2)	6.0 (1)
$(\Delta/\sigma)_{max}$	0.4 × 10^{-4}	0.8 × 10^{-4}	0.5 × 10^{-4}	0.2 × 10^{-4}
$\Delta\rho$, min.; max. (e Å^{-3})	−39.1; 19.6	−57.1; 27.3	−69.7; 32.8	−72.1; 22.5
$\sigma(\Delta\rho)$** (e Å^{-3})	0.10	0.24	0.22	0.15

† The BL14A four-circle diffractometer (Satow & Iitaka, 1989) at the Tsukuba Photon Factory, Japan. ‡ As proposed by Maslen & Spadaccini (1993). § $F_o = yF_k$, where F_k is the value of the kinematic structure factor. ¶ Zachariasen (1967) extinction corrections included in least-squares structure refinement (Larson, 1970). ** Mean e.s.d. value (Cruickshank, 1949).

$\Delta\rho$ maps for all data sets, being biased strongly by the extinction corrections and the scale factor, were also discordant.

Negative atomic charges for cations calculated by partitioning $\Delta\rho$ maps (Hirshfeld, 1977) listed in Table 4 suggest that optimizing extinction along with the structural model overcorrects the strong structure factors. These structure refinements were dominated by highly weighted low-angle reflections and the $|F_o - F_c|/\sigma$ values for the SR data ranged up to 350. Least-squares predictions can have significant bias if the observed data differ from the model far more frequently than predicted for normal distributions. The resulting artefacts in $\Delta\rho$ maps can change a structure's polarity (Streltsov & Maslen, 1992; Maslen *et al.*, 1993, 1994; du Boulay *et al.*, 1995). The extinction parameter correlates so strongly with the least-squares scale factor that optimizing both together reduces the low-angle residuals dramatically.

Bias was alleviated by determining the scale and extinction separately (Refinement 2 in Table 1). A scale was determined first by refining the structure excluding extinction, using unit weights but omitting the 14 reflections most strongly affected by extinction, with $\sin\theta/\lambda < 0.25$ Å^{-1}. With the scale fixed at the first stage value, the extinction parameter and 16 independent

structural parameters, including all anisotropic vibration tensor elements, were determined by full-matrix least-squares refinement of $|F|$ with all measured structure factors weighted by $1/\sigma^2(F_o)$. The reduced extinction corrections for the SR data from Ho_2O_3 (Table 1) indicated by this procedure are close to the Maslen & Spadaccini (1993) algorithm values, increasing our confidence in the extinction and scale evaluated separately in Refinement 2.

3. Structural parameters

Atomic positions for all data sets (Refinement 2) are listed in Table 2.* The Y_2O_3 values are within the range of neutron powder diffraction studies by Faucher (1980), of the X-ray Rietveld analysis by Riello, Fagherazzi, Clemente & Canton (1995) and of single-crystal X-ray diffraction studies by Kevorkov, Karyagin, Munchaev, Uyukin, Bolotina, Chernaya, Bagdasarov & Simonov (1995). The *C*-type oxide structure in Fig. 1 is related to the cubic CaF_2 structure. Eight-coordinated Ca cations in the fluorine cubes reduce to six for RE cations in the *C*-type oxides.

The twofold axis is parallel to **a**. Selected bond lengths for the SR data are set out in Table 3. Each O anion is surrounded tetrahedrally by one RE1 and three RE2 cations. The four neighbours remain almost equidistant in the distorted tetrahedron. Mean RE2—O distances, 2.281 (2), 2.298 (2) and 2.284 (3) Å for Y_2O_3, Dy_2O_3 and Ho_2O_3, respectively, are within 1 e.s.d. of the RE1—O distances in Table 3, as observed for Y_2O_3, In_2O_3 and Sc_2O_3 by O'Connor & Valentine (1969). The 2.250 (8) and 2.263 (4) Å RE1—O distances for Yb_2O_3 and Er_2O_3 at room temperature (Saiki, Ishizawa, Mizutani & Kato, 1985) also closely resemble the corresponding mean values of 2.246 (8) and 2.276 (4) Å. The 2.271 (9) Å RE1—O distance for Er_2O_3 (Malinovskii &

* Lists of structure factors for the four data sets and $\Delta\rho$ maps in the plane with sixfold coordination for the Ho_2O_3 tube data set have been deposited with the IUCr (Reference: AS0696). Copies may be obtained through The Managing Editor, International Union of Crystallography, 5 Abbey Square, Chester CH1 2HU, England.

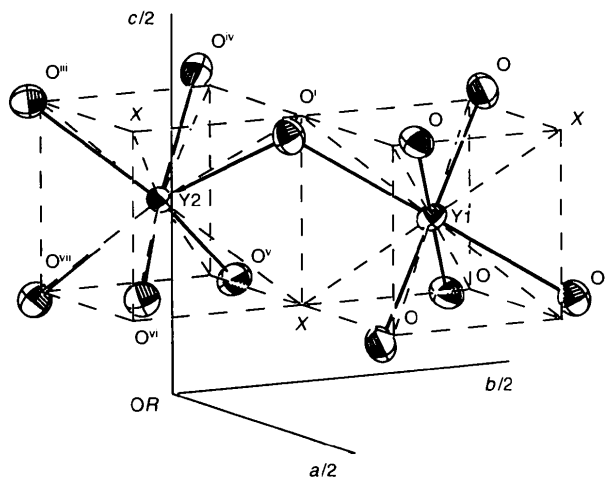

Fig. 1. Oxygen coordination of Y1 in 8(*b*) and Y2 in 24(*d*) cation sites in Y_2O_3. Vibrational ellipsoids at 99% probability level. Dashed lines indicate ideal cube coordination.

Table 2. *Fractional coordinates and anisotropic vibration parameters (U_{ij}, Å^2) with e.s.d.s in parentheses for Y_2O_3, Dy_2O_3 and Ho_2O_3*

The temperature factor has the expression $T = \exp[-2\pi^2(U_{11}(ha^*)^2 + \ldots + 2U_{12}ha^*kb^* + \ldots)]$.

	Y_2O_3 SR	Dy_2O_3 SR	Ho_2O_3 SR	Ho_2O_3 Mo $K\alpha$
x (RE2)	−0.03236 (3)	−0.03163 (2)	−0.03199 (2)	−0.03184 (6)
x (O)	0.3907 (2)	0.3905 (2)	0.3908 (3)	0.3913 (6)
y (O)	0.1518 (2)	0.1516 (2)	0.1516 (2)	0.1512 (6)
z (O)	0.3801 (2)	0.3802 (2)	0.3798 (2)	0.3798 (6)
U_{11} (RE1)	0.0032 (1)	0.00356 (7)	0.00378 (7)	0.0041 (1)
U_{12} (RE1)	0.00056 (7)	0.00074 (4)	0.00066 (4)	0.0008 (1)
U_{11} (RE2)	0.0027 (1)	0.00307 (7)	0.00300 (8)	0.0028 (2)
U_{22} (RE2)	0.0027 (1)	0.00293 (8)	0.00301 (8)	0.0025 (2)
U_{33} (RE2)	0.0027 (1)	0.00304 (8)	0.00308 (8)	0.0025 (2)
U_{23} (RE2)	−0.00026 (6)	−0.00041 (4)	−0.00035 (4)	−0.0004 (1)
U_{11} (O)	0.0051 (5)	0.0055 (5)	0.0061 (7)	0.006 (2)
U_{22} (O)	0.0053 (5)	0.0054 (5)	0.0053 (6)	0.006 (2)
U_{33} (O)	0.0041 (5)	0.0044 (5)	0.0049 (6)	0.004 (2)
U_{12} (O)	−0.0003 (4)	−0.0009 (5)	−0.0004 (5)	0.00 (2)
U_{13} (O)	−0.0006 (4)	−0.0007 (5)	−0.0011 (5)	−0.00 (2)
U_{23} (O)	−0.0005 (4)	−0.0010 (5)	−0.0006 (5)	−0.001 (2)

Table 3. *Selected interatomic distances (Å) and angles (°) for Y_2O_3, Dy_2O_3 and Ho_2O_3 SR data sets*

	Y_2O_3	Dy_2O_3	Ho_2O_3
$RE1O_6$			
(6) RE1—O	2.282 (2)	2.298 (2)	2.283 (3)
(6) O—O^{i}	2.925 (3)	2.943 (3)	2.924 (4)
(6) O—O^{ii}	3.504 (3)	3.530 (3)	3.508 (4)
(6) O—RE1—O^{i}	79.71 (7)	79.64 (8)	79.62 (9)
$RE2O_6$			
(2) RE2—O^{i}	2.242 (2)	2.254 (2)	2.244 (3)
(2) RE2—O^{iii}	2.270 (2)	2.289 (2)	2.270 (3)
(2) RE2—O^{iv}	2.333 (2)	2.350 (2)	2.337 (3)
(4) O^{iv}—O^{iii}	2.917 (3)	2.933 (3)	2.920 (4)
(2) O^{iv}—O^{v}	2.925 (3)	2.943 (3)	2.924 (4)
(1) O^{i}—O^{vi}	3.114 (3)	3.142 (3)	3.119 (4)
(2) O^{i}—O^{v}	3.458 (3)	3.484 (3)	3.462 (4)
(2) O^{i}—O^{iii}	3.697 (3)	3.724 (3)	3.700 (4)
(1) O^{iv}—O^{vii}	3.919 (3)	3.940 (3)	3.926 (4)
(1) O^{iii}—O^{v}	4.238 (3)	4.265 (3)	4.234 (4)
(1) O^{i}—RE2—O^{vi}	87.94 (7)	88.38 (8)	88.03 (9)
(1) O^{iv}—RE2—O^{vii}	114.27 (7)	113.96 (8)	114.89 (7)
(1) O^{iii}—RE2—O^{v}	137.92 (7)	137.80 (6)	137.73 (7)
(6) RE1—RE2^{viii}	3.5129 (3)	3.5420 (2)	3.5180 (5)
(6) RE1—RE2	3.9969 (3)	4.0184 (2)	3.9970 (6)
(4) RE2—RE2^{ix}	3.5296 (3)	3.5581 (2)	3.5343 (5)
(4) RE2—RE2^{ii}	4.0115 (3)	4.0325 (2)	4.0114 (6)

Symmetry codes: (i) $\frac{1}{2}-x, \frac{1}{2}-y, \frac{1}{2}-z$; (ii) x, y, z; (iii) $x-\frac{1}{2}, -y, z$; (iv) $x, -y, \frac{1}{2}-z$; (v) $x-\frac{1}{2}, y, \frac{1}{2}-z$; (vi) $x-\frac{1}{2}, y, \frac{1}{2}-z$; (vii) $\frac{1}{2}-x, -y, z-\frac{1}{2}$; (viii) $-x, \frac{1}{2}+y, \frac{1}{2}-z$; (ix) $-x, -y, -z$.

Bondareva, 1991) is likewise close to the mean RE2—O distance of 2.266 (9) Å. The value $0.2154a$ (O'Connor & Valentine, 1969; Geller, Romo & Remeika, 1967) predicts the mean RE—O distances accurately for all *C*-type RE oxides.

12 RE2 cations form a coordination polyhedron around RE1 with six RE1—RE2 and six of the shortest RE1—RE2^{viii} interatomic distances from Table 3. The RE2 cation coordination polyhedron is formed by four RE1 and eight RE2 cations with two RE1—RE2^{viii}, two RE1—RE2, four RE2—RE2^{ix} and four RE2—RE2^{ii} distances from the central RE2 atom. Displacement of the atoms from the ideal positions in the *C*-type oxides (Fig. 1) lengthens the O—O contacts, whereas some RE—RE vectors are shorter than those in the ideal structure.

The cations in *C*-type RE oxides occupy 8(*b*) $(\frac{1}{4},\frac{1}{4},\frac{1}{4})$ and 24(*d*) $(x,0,\frac{1}{4})$ Wyckoff positions. The 48 O atoms are in general positions. Both crystallographically independent cations are at centres of slightly deformed cubes with six of the eight corners occupied by O atoms. Around RE1 (Y1 in Fig.1) cations in 8(*b*) sites the two unoccupied *X* positions are along the body diagonal. The $\bar{3}$-fold axis is along the line O*R*—*X*—Y1—*X* and the six RE1—O distances are equivalent. Around the RE2 (Y2 in Fig.1) cation in 24(*d*), the unoccupied *X* positions are on the face diagonal. There are three non-equivalent pairs of RE2—O distances. The equal RE2—O^{i} and RE2—O^{vi} vectors directed towards the face with O vacancies enclose the smallest O^{i}—RE2—O^{vi} angle. Displacement of the O^{iii} and O^{v} atoms towards the *X* vacancies at the RE2—O^{iii} distance opens the O^{iii}—RE2—O^{iv} angle, as shown in Table 3.

The Y_2O_3 vibrations are depicted in Fig. 1 as 99% probability ellipsoids. The Mo $K\alpha$ vibration amplitudes measured with the tube X-ray source for Ho_2O_3 are within 3 e.s.d.s of the SR values, although relatively large parameter uncertainties reflect the lower statistical accuracy of the high-angle reflections for that study.

All RE1 atoms vibrate more strongly along the three-fold axis towards *X* vacancies, as noted by Kevorkov *et al.* (1995). The RE2 atom's mean-square amplitudes are slightly less than those for RE1. The RE2 atom vibrations are also less anisotropic, vibrating predominantly towards the *X*—O^{iii} and *X*—O^{v} edges of the RE2 coordination cube in Fig. 1. The O atoms have significant vibration anisotropy, as shown in Table 2. Stronger interaction of the RE2 atom with four of its six near-neighbouring O atoms is also indicated by the RE2—O distances.

4. Atomic charges

Atomic charges (Table 4) were determined by projecting $\Delta\rho$ distributions onto atomic density basis functions (Hirshfeld, 1977). The differences between refinements reflect the charge sensitivity to extinction. Perovskite charges are sensitive to extinction to a degree that increases with the atomic number of the atoms in the structure (du Boulay *et al.*, 1995). The least-squares Refinement 1, with extinction corrections indicated to be 'best' by low *R* factors, is questionable, because the strong extinction reverses the polarity of the atoms. Overestimating extinction can alter polarity spuriously in ionic crystals by increasing the electron count on heavy cations. Electrons are transferred from RE cations towards the O anions by amounts resembling the formal ionic charges. All atom charges for Refinement 2 listed in Table 4 are consistent with the isolated atom electronegativities. Independent support for the SR charges in Ho_2O_3 using the Refinement 2 extinction parameters justifies confidence in their reliability.

Table 4. *Atomic charges in electrons from Hirshfeld partitioning of $\Delta\rho$ for Y_2O_3, Dy_2O_3 and Ho_2O_3*

	Y_2O_3 SR	Dy_2O_3 SR	Ho_2O_3 SR	Ho_2O_3 Mo $K\alpha$
No extinction correction applied				
RE1	4.71 (8)	9.3 (2)	10.0 (4)	9.2 (2)
RE2	4.99 (8)	8.2 (2)	8.3 (4)	7.3 (2)
O	−3.23 (5)	−5.8 (2)	−6.1 (3)	−5.5 (2)
Refinement 1				
RE1	1.53 (7)	−2.5 (1)	−2.9 (3)	−5.5 (1)
RE2	2.15 (7)	−3.8 (1)	−3.4 (4)	−6.5 (2)
O	−1.23 (5)	2.1 (1)	2.1 (3)	4.0 (2)
Refinement 2				
RE1	3.66 (9)	3.0 (2)	3.4 (4)	2.6 (2)
RE2	4.15 (9)	2.4 (2)	2.9 (4)	1.6 (2)
O	−2.60 (6)	−1.8 (1)	−2.1 (3)	−1.4 (2)
Extinction correction as proposed by Maslen & Spadaccini (1993)				
			3.6 (5)	
			3.0 (5)	
			−2.2 (4)	

Although the cation charges for these *C*-type RE sesquioxides are considerably higher than those in the corundum-type structures α-Al_2O_3 (Maslen *et al.*, 1993) and α-Fe_2O_3 (Maslen *et al.*, 1994), the latter compounds are expected, from electronegativity considerations, to be more covalent than RE oxides. Small effective cation charges in these crystals should reduce electrostatic repulsion between neighbouring cations and allow cation–cation contacts across the octahedral face of MO_6 moieties to shorten, as in the corundum structure. Relatively greater cation–cation repulsion would explain why that structure is not stable for RE oxides.

5. Electron density

The $\Delta\rho$ maps discussed below were based on the SR data refinements listed last in Table 1. Each 12-fold coordination polyhedron defined by the cation lattice contains two crystallographically independent sixfold hexagonal sections through the RE1 and RE2 atoms, parallel and perpendicular, respectively, to threefold axes

in these cubic structures. Least-squares plane sections parallel to the threefold axis through central RE1 or RE2 atoms are shown, with six neighbouring cations, in Fig. 2. Least-squares plane sections perpendicular to the twofold axes through fourfold coordinations with RE1 and RE2 atoms are shown in Fig. 3. The smallest $\Delta\rho$ contour interval (1.5 e Å^{-3}) is much greater than the $\sigma(\Delta\rho)$ values listed in Table 1. The other $\Delta\rho$ maps with six- and fourfold coordinations, not reproduced here, do not differ conceptually from Figs. 2 and 3. Corresponding Mo $K\alpha$ data-set maps for Ho_2O_3 reproduce the main features of the electron distribution in Figs. 2 and 3 and are deposited.*

Aspherical $\Delta\rho$ density around the RE sites in Figs. 2 and 3 indicates that the RE-atom prepared states spherical symmetry is not preserved. This also occurs

* See deposition footnote on p. 417.

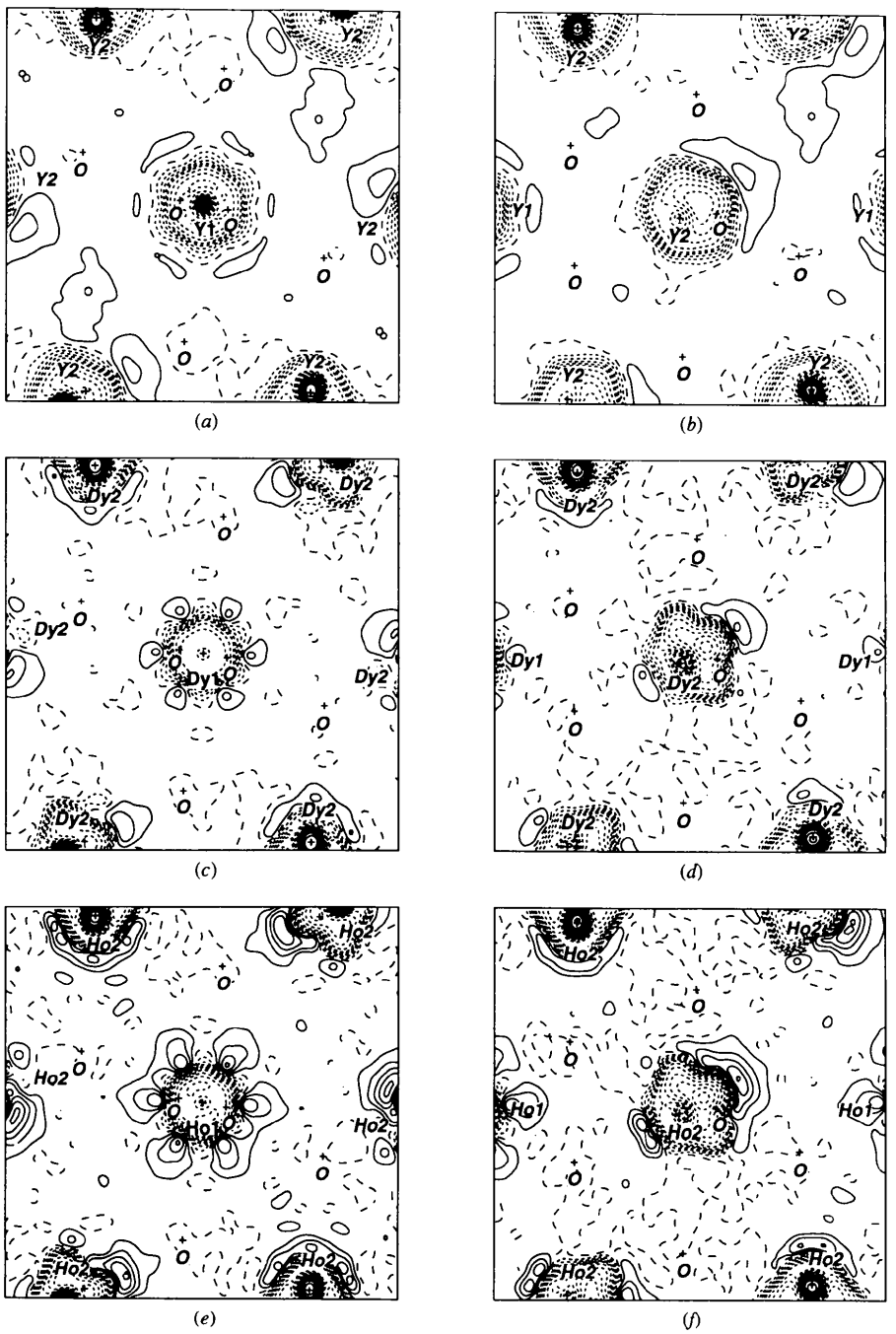

Fig. 2. $\Delta\rho$ maps in the plane with sixfold coordination for RE1 and RE2 atoms in (*a*) and (*b*) Y_2O_3, (*c*) and (*d*) Dy_2O_3, and (*e*) and (*f*) Ho_2O_3. Atoms deviating from the plane are shown in italics. Map borders 6.4 × 6.4 Å. Contour intervals 1.5 e Å^{-3} for $\Delta\rho \leq$ 7.5 e Å^{-3} and 1.5n e Å^{-3}, n = 2, 3,..., for $\Delta\rho >$ 7.5 e Å^{-3}; positive contours solid, negative contours short dashes.

for Y in $YFeO_3$ (du Boulay *et al.*, 1995) and in RE-atom complexes (Chatterjee, Maslen & Watson, 1988).

All $\Delta\rho$ maps follow a remarkably regular progression. Positive features become more prominent from Y_2O_3 to Dy_2O_3 to Ho_2O_3. The local sixfold symmetry of the $\Delta\rho$ density near the RE1 cations in Fig. 2 reflects the sixfold near-neighbour cation–cation geometry. It does not match the local symmetry of the six nearest O atoms, projected onto the plane of Fig. 2 and deviating from that plane by ±2.3, ±0.8 and ±0.4 Å. On the other hand, the lower $\Delta\rho$ map symmetry near the RE2 atom (0.2 Å off the plane) does correspond to the approximate twofold geometry of the neighbouring O atoms, which deviate from the (*b*), (*d*) and (*f*) planes in Fig. 2 by 2.4, 0.8, 2 × –0.7, –0.9 and –1.0 Å. These results imply that six nearest-neighbour O atoms in the low-symmetry (C_2)

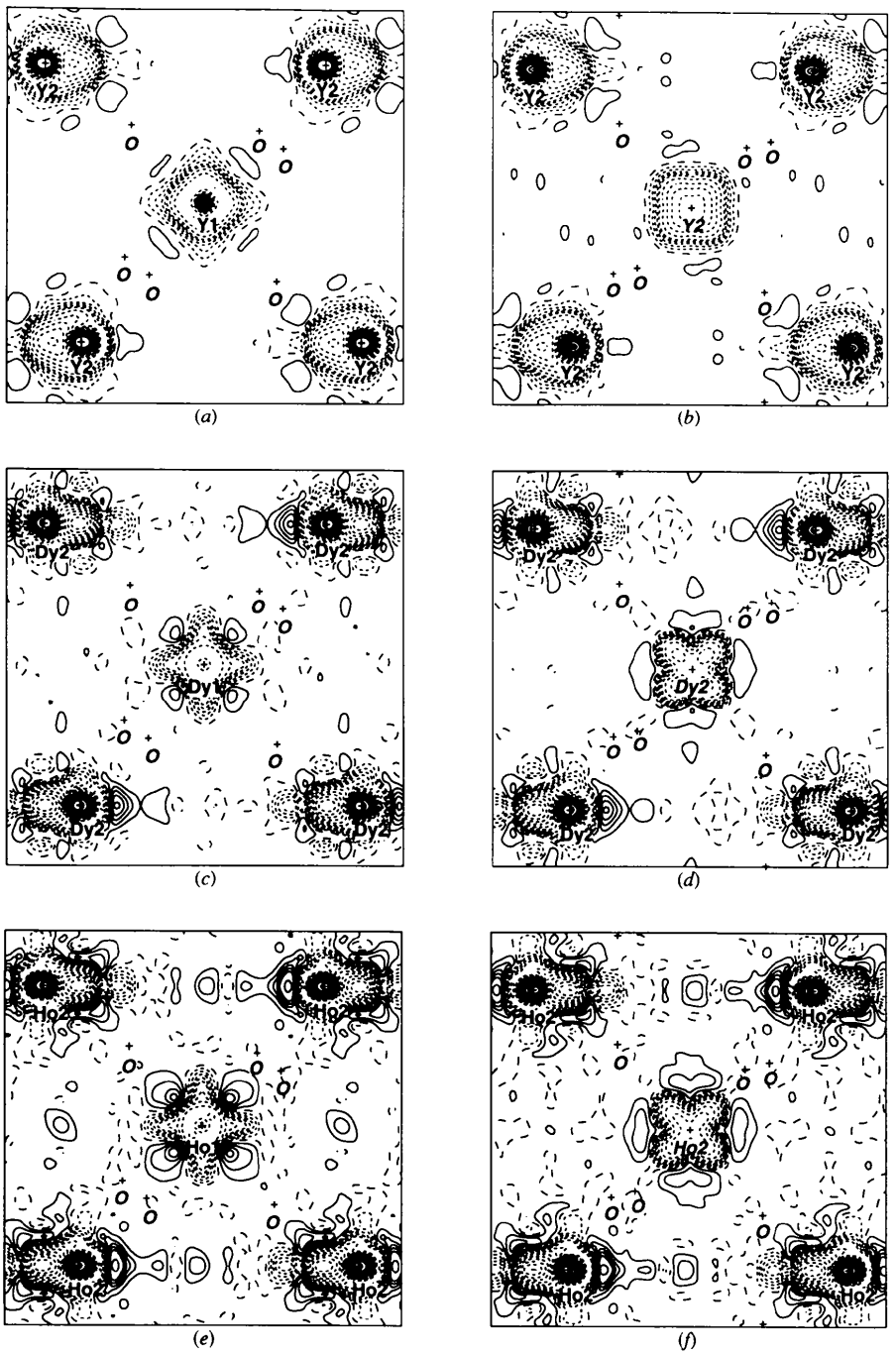

Fig. 3. $\Delta\rho$ maps in the plane with fourfold coordination for RE1 and RE2 atoms in (*a*) and (*b*) Y_2O_3, (*c*) and (*d*) Dy_2O_3, and (*e*) and (*f*) Ho_2O_3. Atoms deviating from the plane are shown in italics. Map borders 7.5 × 7.5 Å. Contours as for Fig. 2.

coordination surrounding RE2 influence the deformation density more strongly than those in trigonally distorted octahedral ($C_{3i} \simeq O_h$) coordination surrounding RE1.

The fourfold local symmetry of the $\Delta\rho$ maps around both the RE1 and RE2 sites in Fig. 3 approximates that of the nearby cations, not the anions. It is higher than the true symmetry. The RE1 atom is on a threefold axis inclined to this plane and RE2 is on a twofold axis perpendicular to Fig. 3. Although the cation geometries around RE1 and RE2 look similar in Fig. 3, the four $\Delta\rho$ density lobes near RE2 are rotated by 45° with respect to those around RE1. Three O atoms are ±1.1, ±1.4 and ±1.5 Å above and below the RE1 cation in Fig. 3. The RE2 cation, 0.3 Å off the plane, has four O atoms 2 × 1.2 Å above and two 2 × −1.3 Å below the plane.

The O atoms in the anion layers around RE2 distort the electron density from the geometry of the interacting cations. There is an obvious local dipole component along the twofold crystallographic axis around each RE2 atom near the corners of the Fig. 3 maps. Each RE2 cation's electron density is polarized towards the next RE2 atom on the twofold axis, which extends through the (4 O) pseudo-cubic face with large O—RE2—O angles. This density is squeezed by the four nearest O atoms into one positive lobe. The electron density on the opposite side of the RE2 cation is depleted strongly by the (2 O + 2 *X*) pseudo-cubic face arrangement with the small O—RE—O angles. The repelled electrons accumulate further from the RE2 nuclei in approximate toroids, slightly polarized through the (2 O + 2 *X*) pseudo-cubic face towards the next RE1, RE2 cation layer, with four positive density lobes around the central RE2 cation arranged as in Fig. 3. This fourfold component reflecting the geometry of the surrounding cations appears to be exactly in the plane of Fig. 3. It is ~0.3 Å from the central RE2 atom and projects into the two 'wings' near the RE2 atoms at the corners of the $\Delta\rho$ maps. The two nearest O atoms on this side of the central RE2 atom force the accumulated fourfold density to rotate by 45° with respect to those around RE1. Thus, interactions of the RE2 atoms' electron density with the next cation neighbours and those with the nearest low-symmetry (C_2) anions are competitive, producing the complex $\Delta\rho$ deformations noted in Fig. 3.

6. Discussion

There is a striking increase in the density of the anisotropic positive features in Figs. 2 and 3 with the number of 4*f* electrons. As the rare earth 4*f* electron sub-shells are characterized by a $< r^2 >^{1/2} \simeq 0.35$ Å radius that is small compared with the ~1 Å radius of the closed $5s^2 5p^6$ sub-shells, one might expect 4*f* electron density to be screened by the 5*s* and 5*p* sub-shells and remain spherically symmetric. The RE atoms in these oxides are separated by ~10 times the 4*f* sub-shell radius. Overlap between 4*f* orbitals centred on neighbouring atoms is correspondingly weak and it is often asserted that 4*f* electrons interact so weakly with the surrounding atoms' electrons that RE atoms in periodic lattices can be treated as independent spherically symmetric ions. This zeroth-order approximation is based on the assumption that the $\Delta\rho$ density is predominantly due to the repopulation of near-degenerate free atomic orbitals.

It can be crudely argued that exchange increases, along with the Coulomb interactions between electrons, as the square of the atomic number, inducing electron correlation that alters the accessible orbitals' energies, but the electron-density redistribution is also field-dependent. The significant asphericity and polarization of the electron density in Figs. 2 and 3 depends not just on the prepared state symmetry, but also on the strength and geometry of the perturbing field.

Perturbation expansions describe atomic charge density polarization in terms of re-population of energy levels (*e.g.* Atkins, 1983). The number of closely spaced levels increases with atomic number. These studies of RE oxides suggest that polarization by occupying higher energy levels is more important than repopulation of 4*f* orbitals. An energy discrepancy for RE oxides modelled by overlapping ground state neutral atoms implies that the electron density migrates away from regions of high electrostatic potential. Electron depletion near the nuclei must predominate in such compounds. The maps shown in Figs. 2 and 3 do indeed show deep negative $\Delta\rho$ density in the vicinity of the RE nuclei.

The three-dimensional electron density near each RE1 atom is characterized by 12 maxima alternating with 12 minima, indicating higher-order multipole contributions to the angular dependence of the density. The sixfold $\Delta\rho$ symmetry near the RE1 cations becomes progressively more prominent from Y to Dy and Ho.

The RE-atoms' 5*d* state energies are close to the 4*f* energies and can reasonably be invoked to describe their bonding. A superexchange mechanism analogous to that for 3*d* compounds described by Anderson (1963) would correspond here to virtual transfer of a 4*f* electron from one site to another *via* the O anion's *p* state. Because overlap between these *p* and 4*f* states is small, it is not surprising that Kasuya (1970) found this mechanism to be too small to account for experimental observations that it was invoked to explain, and proposed other mechanisms for longer range interactions involving *d* and *f* electrons in non-metallic rare earth compounds. One involves virtual transfer of the anion's *p* electron to the 5*d* state of a neighbouring RE cation and alignment of 4*f* spins through *d*–*f* exchange. Such *p*–*d* mixing leads to antiferromagnetic coupling and is more important than a *p*–*f* mechanism due to larger overlap between *p* and 5*d* states. The other mechanisms proposed include categories in which the cation wavefunction is predominant compared with the anion's *p* band. Overlap between next-neighbour cation wavefunctions becomes significant. The 4*f* electrons virtually transferred to 5*d*

states experience the usual *d–f* exchange interaction. Consideration of such interaction mechanisms is justified by the $\Delta\rho$ electron density near the RE1 cations despite *d–f* mixing decreasing very quickly with increasing RE—RE distance.

All the exchange interaction mechanisms proposed for RE oxides lead to ordering temperatures of a few Kelvin. The corresponding magnetic structures are complex. The relative strengths of the crystal field (CF) and magnetic exchange interactions determine the magnetic anisotropy. The $\Delta\rho$ map symmetry near the RE2 cation in Figs. 2 and 3, being lower than expected from cation–cation interactions alone, is presumably affected by the O coordination CF with C_2 symmetry. Because this symmetry is low and the magnetic interactions are smaller than the energy of the first excited CF level, the magnetic behaviour is dominated by the CF anisotropy. The magnetic structure, even for simple antiferromagnetic interactions, can be complex and non-collinear. This occurs in RE oxides, where the unit cell contains two cation sites, for one of which (RE2) the (C_2) crystal field has a strong influence on the $\Delta\rho$ maps. A non-collinear structure is more probable if the RE site symmetry is low enough. This also occurs in RE perovskites (C_s) and in RE garnets (C_{2v}).

Thus, the main topological characteristics of the deformation density for the heavier members of the series can be broadly related to exchange effects responsible for the Pauli principle and to the field-dependent energy-level structure of the RE sesquioxides.

This work was supported by the Australian Research Council. Financial support of the Australian National Beamline Facility (ANBF) is also acknowledged. The ANBF is funded by a consortium comprising the ARC, DITARD, ANSTO, CSIRO, ANU and UNSW. We are indebted to Dr N. R. Streltsova for assistance in growing crystals and in data collection.

References

Alcock, N. W. (1974). *Acta Cryst.* A**30**, 332–335.
Anderson, P. W. (1963). *Magnetism I*, edited by G. T. Rado & H. Suhl, pp. 25–83. New York, London: Academic Press.
Atkins, P. W. (1983). *Molecular Quantum Mechanics*, 2nd ed. Oxford University Press.
Boulay, D. du., Maslen, E. N., Streltsov, V. A. & Ishizawa, N. (1995). *Acta Cryst.* B**51**, 921–929.
Chatterjee, A., Maslen, E. N. & Watson, K. J. (1988). *Acta Cryst.* B**44**, 386–395.
Creagh, D. C. (1992). Private communication.
Cruickshank, D. W. (1949). *Acta Cryst.* **2**, 65–82.
Faucher, M. (1980). *Acta Cryst.* B**36**, 3209–3211.
Garton, G. & Wanklyn, B. M. (1968). *J. Mat. Sci.* **3**, 395–401.
Geller, S., Romo, P. & Remeika, J. P. (1967). *Z. Kristallogr.* **124**, 136–142.
Hall, S. R., Flack, H. D. & Stewart, J. M. (1992). *Xtal*3.2 *Reference Manual*. Universities of Western Australia, Australia, and Maryland, USA.
Hester, J. R., Maslen, E. N., Spadaccini, N., Ishizawa, N. & Satow, Y. (1993). *Acta Cryst.* B**49**, 967–973.
Hirshfeld, F. L. (1977). *Isr. J. Chem.* **16**, 198–201.
Kasuya, T. (1970). *IBM J. Res. Dev.* **14**, 214–223.
Kevorkov, A. M., Karyagin, V. F., Munchaev, A. I., Uyukin, E. M., Bolotina, N. B., Chernaya, T. S., Bagdasarov, Kh. S. & Simonov, V. I. (1995). *Cryst. Rep.* **40**(1), 23–26.
Larson, A. C. (1970). *Crystallographic Computing*, edited by F. R. Ahmed. Copenhagen: Munksgaard.
Malinovskii, Yu. A. & Bondareva, O. S. (1991). *Sov. Phys. Cryst.* **36**(6), 882–883.
Maslen, E. N. & Spadaccini, N. (1993). *Acta Cryst.* A**49**, 661–667.
Maslen, E. N., Streltsov, V. A., Streltsova, N. R. & Ishizawa, N. (1994). *Acta Cryst.* B**50**, 435–441.
Maslen, E. N., Streltsov, V. A., Streltsova, N. R., Ishizawa, N. & Satow, Y. (1993). *Acta Cryst.* B**49**, 973–980.
O'Connor, B. H. & Valentine, T. M. (1969). *Acta Cryst.* B**25**, 2140–2144.
Rees, B. (1977). *Isr. J. Chem.* **16**, 180–186.
Riello, P., Fagherazzi, G., Clemente, D. & Canton, P. (1995). *J. Appl. Cryst.* **28**, 115–120.
Saiki, A., Ishizawa, N., Mizutani, N. & Kato, M. (1985). *Yogyo Kyokai Shi*, **93**(10), 649–654.
Satow, Y. & Iitaka, Y. (1989). *Rev. Sci. Instrum.* **60**, 2390–2393.
Streltsov, V. A. & Maslen, E. N. (1992). *Acta Cryst.* A**48**, 651–653.
Streltsov, V. A. & Zavodnik, V. E. (1989). *Sov. Phys. Cryst.* **34**(6), 824–828.
Zachariasen, W. H. (1967). *Acta Cryst.* A**23**, 558–564.